

# Inverse design of arbitrary optical helicity patterns.

Romuald Kilianski\* and Robert Bennett

*University of Glasgow*

*University Avenue*

*G12 8QQ, Glasgow*

(Dated: November 29, 2022)

Superposing multiple plane waves can generate helicity lattices, in which the optical helicity varies regularly in space. Here we propose an inverse design method for constructing arbitrary helicity structures based on placing a digital structure of dielectric inclusions in three-dimensional space. We apply the method to design structures that reproduce two-dimensional lattices embedded within a three-dimensional region using only a single plane wave as an input. In order to demonstrate the power and flexibility of our method, we go beyond the paradigm of a regular lattice and propose structures which can create arbitrary images consisting of regions of varying helicity, again using only a single plane wave as an input.

## I. INTRODUCTION

Helicity lattices are periodic optical structures resembling the arrangement of intensity patterns of optical trapping potentials. They are formed by the superposition of non-interfering plane waves [1] and can be constructed such that the mean square of the electric field is homogeneous. The term helicity density originated in plasma physics [2], and for monochromatic light is proportional to its chirality (handedness). The concept of chirality appears across the sciences and details the characteristics of geometrical arrangements, which could be abstract objects or biomolecules with identical properties but inverted (non-superimposable) forms. This appears in optics via optical helicity, arising from the interpretation of light's angular momentum associated with its circular polarization [3]. The sensitivity with which enantiomers (molecular species of opposite handedness) can be distinguished is of central importance in areas such as pharmacology. The various methods of doing so [4] often include optical dichroism, exploiting the relationship between chiral molecule's absorption cross sections and a circularly polarised light [5]. Moreover, recently a scheme was proposed to utilize helicity lattices in separating cold, chiral molecules [6], where the alternating helicity regions exert a force on enantiomers, giving rise to novel quantum phases. With its potential in applications as well as a tool for probing new physics, helicity lattices and their systematic integrated generation will likely become important.

The need to design a method that manipulates light and is able to produce a helicity lattice suggests exploring the catalogue of techniques of photonics. Looking from a historical perspective, the shift into smaller-scale engineering of electronic and photonic devices had a great impact on the science of light wave manipulation [7]. Progressively undergoing since the 1960s, it introduced the possibility of fabrication of devices in a micro and

nano-scale regime (the order of a wavelength of visible light or smaller). With the greater availability and accessibility of computing power, the late 90s saw the introduction of inverse design (ID), structure-building algorithms, where the desired end goal that the structure achieves is specified *a priori*. The methods employed there fall into two categories: generic (evolutionary) [8] and gradient-based [9]. The former was initially exemplified by the design and fabrication of a telecom-fibre to ridge-waveguide coupler [10], the latter, by a bandgap optimization with the use of a gradient algorithm [11]. These designs, along with some of their successors [12] relied on intuition and drew from a pool of familiar geometrical shapes. In a typical problem, the sizes and positions of fixed circles and rectangles would be altered, and given these constraints, an optimization could be performed. Finding an optimum design in such a case may be relatively straightforward however, the increase in performance is limited as the constrained optimization is unlikely to reach a global maximum. The beginning of the 2000s saw an expansion of ID in applications such as waveguide bends [13], wave multiplexers on a wavelength scale [14] and the creation of wide bandgaps with the aid of different photonic crystal (PhC) configurations [15]. This era also saw an introduction of adjoint methods; the origin of which lies in computational techniques originally developed in aerospace design [16]. One of the consequences of the adjoint density formalism [17, 18] was a shift into free-form optimization. The pool of available designs was now unlimited and the shapes of the structures were dictated by their impact on performance and no longer guided by intuition. The scheme has also improved the computational efficiency of ID and enlarged the space of its possible applications. Since then, ID has been applied to problems with greater complexity. Some of the recent applications were concerned with: the conversion of solar energy [19], integrated photonics devices [20], subwavelength focusing [21] and heat transfer [22]. Most recently, ID has been applied to atomic coherence [23], light-matter interactions [24] and nuclear quantum optics [25].

It has been shown analytically that helicity lattices

---

\* email: r.kilianski.1@research.gla.ac.uk

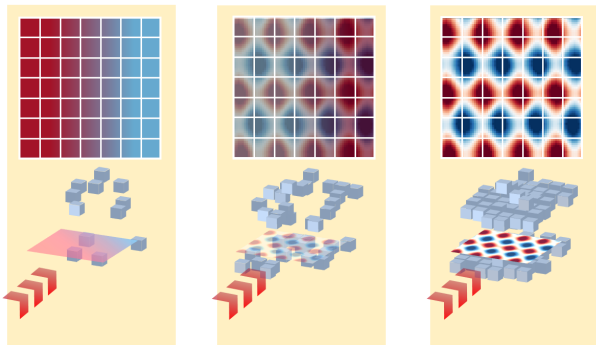


FIG. 1. The schematic of different stages of building the dielectric structure using a single beam source. As it grows in size and complexity, the more the underlying field approximates the helicity lattice.

can be constructed from up to six non-interfering plane waves [1] in various configurations. The multi-beam requirement of these structures motivates us to design a procedure capable of reproducing the helicity lattice but requiring fewer light sources. By using a single beam as an input, the setup becomes less susceptible to error arising from adjustment or alignment, thus reducing the complexity of the task, rendering the scheme more robust. To accomplish this, we require a dielectric structure that can refract a single beam multiple times in such a way that a lattice structure emerges in a given plane. The placement of the elements forming such a structure is non-obvious and cannot be inferred from a wave analysis point of view. Hence, we adopt an approach based on freeform inverse design, where the desired outcome or a set of outcomes is chosen and an algorithm adjusts the initial conditions (specific geometry) to meet the designated goal. The solutions to such problems are not unique, hence a solution closest to the original goal is chosen. This recasts the problem as an optimization task. In this paper, we put forward a proof of principle describing a method of efficient generation of multi-wave helicity lattices using a single beam.

This paper is organized as follows: firstly, we frame the problem of helicity lattice generation in terms of an optimization task, develop the mathematical structure and propose an algorithm capable of reproducing a helicity lattice. We then outline the specifics of the actual inverse design process. Subsequently, we proceed to present the results of two different simulations (reproducing lattices originally formed by a superposition of three sources in alternative configurations). Additionally, we present a novel approach where we simulate a helicity density that is not periodic and can take an arbitrary (user-defined) shape.

## II. DESCRIPTION OF THE PROBLEM

We aim to produce a two-dimensional optical pattern resembling a helicity lattice. Instead of superposing multiple light sources, we want to effect it by shining a single beam onto a crystal-like (not uniformly periodic) structure that will refract the beam in such a way that the helicity pattern emerges in a specified location. Our goal is to create such a structure algorithmically; instead of iterating over possible geometries, we let an algorithm grow the shape of the crystal. At every step, the algorithm decides on the optimal placement of a cube of dielectric material. To choose the optimal placement of dielectric inclusions, an inverse design algorithm based on the adjoint method is used.

Utilizing the explicit forms of electric and magnetic fields, we employ an approach called shape calculus which is established on the understanding of the relationship between Maxwell's equations and small changes in geometry [26]. In our present problem, this manifests as the link between introducing small blocks of dielectric material and their effect on the existing electric and magnetic fields. We aim to bring the fields into a form such that they produce a two-dimensional helicity lattice.

By using the form of Maxwell's equations without sources (keeping in mind that we will need to explicitly specify the polarization  $\mathbf{P}$  and magnetization  $\mathbf{M}$  density respectively), we can explore the symmetries between source and observation points. Following [27], we write the Fourier transformed Maxwell equations as:

$$\nabla \cdot \varepsilon \mathbf{E} = 0 \quad (1)$$

$$\nabla \cdot \mu \mathbf{H} = -\nabla \cdot \mu_0 \mathbf{M} \quad (2)$$

$$\nabla \times \mathbf{E} = -i\omega \mu \mathbf{H} \quad (3)$$

$$\nabla \times \mathbf{H} = i\omega \varepsilon \mathbf{E}, \quad (4)$$

where  $\varepsilon$  and  $\mu$  are permittivity and permeability respectively. Using constitutive relations  $\mathbf{D} = \varepsilon \mathbf{P}$ ,  $\mathbf{B} = \mu \mathbf{H} + \mu_0 \mathbf{M}$ , we can express the relationship between electric and magnetic fields and polarization and magnetization in an explicit way:

$$[\nabla \times \mu^{-1} \nabla \times -\omega^2 \varepsilon] \mathbf{E} = \omega^2 \mathbf{P} - i\omega \mu_0 \nabla \times \mu^{-1} \mathbf{M} \quad (5)$$

$$[\nabla \times \mu^{-1} \nabla \times -\omega^2 \varepsilon] \mathbf{H} = i\omega \nabla \times \varepsilon^{-1} \mathbf{P} + \mu_0 \omega^2 \mathbf{M}. \quad (6)$$

The correspondence between the sources in terms of Green's tensors has been derived in [27], thus we are going to state the important results which form the foundational symmetry argument in the case of the adjoint method. The components of a Green's tensor describing an electric field radiating from an electric dipole,  $\mathcal{G}_{ij}^{EP}$  are combinations of vector components of the form  $\hat{e}_i E_j$ , where  $\hat{e}$  is an electric dipole moment vector. Analogously, the elements of a Green's tensor relating magnetic source with its field,  $\mathcal{G}_{ij}^{HM}$  are  $\hat{m}_i H_j$ , where  $\hat{m}$  is a magnetic dipole moment vector. We can express the source-observer symmetry in reciprocal media in terms

of  $\mathcal{G}^{EP/HM}$  as:

$$\mathcal{G}_{ij}^{EP/HM}(\mathbf{r}_2, \mathbf{r}_1) = \mathcal{G}_{ji}^{EP/HM}(\mathbf{r}_1, \mathbf{r}_2). \quad (7)$$

The  $i$ -th component of an electric/magnetic field at  $\mathbf{r}_2$  arising from the  $j$ -th component of an electric/magnetic dipole at  $\mathbf{r}_1$  is equal to the  $j$ -th component of an electric/magnetic field at  $\mathbf{r}_1$  from the  $i$ -th component of an electric/magnetic dipole at  $\mathbf{r}_2$ . This relation shows that a purely electric or magnetic source can be exchanged with its respective field at the observation point. The relationship is not so straightforward for an electric/magnetic field radiating from a magnetic/electric dipole. If we let  $\mathcal{G}_{ij}^{HP}$  define a Green's tensor encapsulating a magnetic field from an electric dipole, and  $\mathcal{G}_{ij}^{EM}$  be containing an electric field from a magnetic dipole, the relation reads:

$$\mathcal{G}_{ij}^{EM}(\mathbf{r}_2, \mathbf{r}_1) = -\mathcal{G}_{ji}^{HP}(\mathbf{r}_1, \mathbf{r}_2). \quad (8)$$

Equations (7) and (8) enable us to simplify the expression describing the interplay between the fields and our goal structure. This is discussed in detail in the next section.

### A. Choosing a merit function

The analytical expression for the monochromatic helicity density as defined in [1] reads

$$\mathcal{H} = -\frac{i}{4c\omega} (\mathbf{E} \cdot \mathbf{H}^* - \mathbf{E}^* \cdot \mathbf{H}). \quad (9)$$

To create an algorithm capable of creating a helicity lattice with a desired geometrical pattern, we need to choose a merit function (a function that can output a number that encodes the closeness of a given field to the goal), which we will aim to optimize. Inspired by [28], a method of controlling 3D optical fields and their intensity, we seek to gain control of the value of helicity density at points in 3D space. Since we possess a goal pattern  $\mathcal{H}_0$ , and know the field values that create it, a natural choice would be to define a set  $S$  of  $N$  critical points where  $\mathcal{H}_0$  takes maximum and minimum values. A simulated helicity density  $\mathcal{H}[\mathbf{E}, \mathbf{H}]$  can be compared with the values  $\mathcal{H}_0$  takes at these coordinates, hence a measure of similarity between the two fields can be established. The merit function  $\Theta[\mathbf{E}, \mathbf{H}]$  will take the form:

$$\Theta[\mathbf{E}, \mathbf{H}] = \sum_{\substack{k=1, \\ \mathbf{s}_k \in S}}^N \{\mathcal{H}_0(\mathbf{s}_k) - \mathcal{H}[\mathbf{E}, \mathbf{H}](\mathbf{s}_k)\}^2. \quad (10)$$

The closer  $\Theta$  is to zero, the closer  $\mathcal{H}[\mathbf{E}, \mathbf{H}]$  will approximate the desired pattern  $\mathcal{H}_0$ . The change in  $\Theta$  will be

given by:

$$\begin{aligned} \delta\Theta[\mathbf{E}, \mathbf{H}] &= 2 \sum_{\substack{k=1, \\ \mathbf{s}_k \in S}}^N \{\mathcal{H}_0(\mathbf{s}_k) - \mathcal{H}[\mathbf{E}, \mathbf{H}](\mathbf{s}_k)\} \delta\mathcal{H}[\mathbf{E}, \mathbf{H}](\mathbf{s}_k) \\ &= 2 \sum_{\substack{k=1, \\ \mathbf{s}_k \in S}}^N \Delta\mathcal{H}(\mathbf{s}_k) \delta\mathcal{H}[\mathbf{E}, \mathbf{H}](\mathbf{s}_k) \end{aligned} \quad (11)$$

where we defined  $\Delta\mathcal{H}(\mathbf{s}_k) \equiv \mathcal{H}_0(\mathbf{s}_k) - \mathcal{H}[\mathbf{E}, \mathbf{H}](\mathbf{s}_k)$ . We want to evaluate the  $\delta\mathcal{H}[\mathbf{E}, \mathbf{H}]$  at each site in  $S$ . The variation at a site  $\mathbf{r}_p$  will read:

$$\delta\mathcal{H}[\mathbf{E}, \mathbf{H}](\mathbf{r}_p) = \text{Re} \{ \mathbf{H}^*(\mathbf{r}_p) \delta\mathbf{E}(\mathbf{r}_p) - \mathbf{E}^*(\mathbf{r}_p) \delta\mathbf{H}(\mathbf{r}_p) \}. \quad (12)$$

The variations in the fields  $\mathbf{E}$  and  $\mathbf{H}$  are given by a product of a Green's tensor  $\mathcal{G}$  with a source current  $\mathbf{P}$

$$\delta\mathbf{E}(\mathbf{r}_p) = \int_{\phi} d^3\mathbf{r} \mathcal{G}^{EP}(\mathbf{r}, \mathbf{r}_p) \mathbf{P}(\mathbf{r}_p) \quad (13)$$

$$\delta\mathbf{H}(\mathbf{r}_p) = \int_{\phi} d^3\mathbf{r} \mathcal{G}^{HP}(\mathbf{r}, \mathbf{r}_p) \mathbf{P}(\mathbf{r}_p), \quad (14)$$

where  $\phi$  is a 3D region containing the inclusion. Taking to account the reciprocity relations (7) and (8), we can write the variation in  $\Theta$  at a point  $\mathbf{p}$  as:

$$\delta\Theta[\mathbf{E}, \mathbf{H}](\mathbf{s}_p) = 2 \int_{\phi} d^3\mathbf{r} \text{Re} \{ \mathbf{P}(\mathbf{r}) \cdot \mathbf{F}_p(\mathbf{r}, \mathbf{s}_p) \}, \quad (15)$$

where we defined  $\mathbf{F}_p(\mathbf{r}, \mathbf{s}_p)$  as

$$[\mathbf{H}^*(\mathbf{s}_p) \mathcal{G}^{EP}(\mathbf{r}, \mathbf{s}_p) + \mathbf{E}^*(\mathbf{s}_p) \mathcal{G}^{EM}(\mathbf{r}, \mathbf{s}_p)] \Delta\mathcal{H}(\mathbf{s}_p). \quad (16)$$

$\mathbf{F}_p(\mathbf{r}, \mathbf{s}_p)$  is the adjoint field originating at the point  $\mathbf{s}_p$ , measured at  $\mathbf{r}$ .  $\mathbf{P}(\mathbf{r})$  is the polarization density induced by placing a cube of dielectric material at  $\mathbf{r}$ . Since the inclusion's permittivity  $\varepsilon_I$  is isotropic,  $\mathbf{P}(\mathbf{r})$  can be written as a total dipole moment  $(\varepsilon_I - \varepsilon_1) a^3 \mathbb{I} \mathbf{E}(\mathbf{r})$ , where  $a$  is the side length of the inclusion,  $\varepsilon_1$  is the permittivity of the medium and  $\mathbb{I}$  is the unit matrix. We are only interested in relative changes in the merit function between sites, therefore the scalar permittivity prefactor can be ignored by noting that  $\mathbf{P}(\mathbf{r}) \propto \mathbf{E}(\mathbf{r})$ . The simplified variation in  $\Theta$  at a site  $\mathbf{r}_p$  then reads:

$$\delta\Theta[\mathbf{E}, \mathbf{H}](\mathbf{s}_p) \approx \text{Re} \{ \mathbf{E}(\mathbf{r}) \cdot \mathbf{F}_p(\mathbf{r}, \mathbf{s}_p) \}, \quad (17)$$

making the total variation:

$$\begin{aligned} \delta\Theta[\mathbf{E}, \mathbf{H}] &\approx \text{Re} \left\{ \mathbf{E}(\mathbf{r}) \cdot \sum_p^N \mathbf{F}_p(\mathbf{r}, \mathbf{s}_p) \right\} \\ &= \text{Re} \{ \mathbf{E}(\mathbf{r}) \cdot \mathbf{F}(\mathbf{r}) \} \end{aligned} \quad (18)$$

The change (variation) in the merit function  $\Theta$  is thus given by the overlap between the real field  $\mathbf{E}$  and the adjoint field  $\mathbf{F}$ .

## B. Advantages of adjoint method over brute force optimization

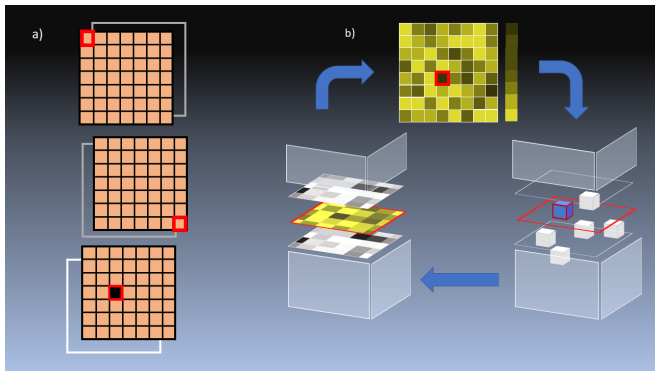


FIG. 2. A brute-force optimization in a) and adjoint method in b). In a) the algorithm has to iterate through every coordinate in 3D space placing a test inclusion there and running a separate simulation before it can determine the optimal location. In b) the adjoint method finds this coordinate by doing only two simulations. Both a) and b) continue until the merit function value can no longer decrease.

To find a structure producing a helicity lattice one might either use intuition or follow a brute force process of building it. This involves trying every coordinate one-by-one, and measuring what effects placing the inclusion there, has on the merit function. One then would narrow it down to the single coordinate where the dielectric block exerts the largest influence, and place it there. The whole procedure would have to be repeated for every element added to the structure until the goal field is reached. For a 3D simulation, it would require a number of iterations equal to the number of blocks needed to reach the goal, multiplied by  $n^3$ , where  $n$  is the number of grid points along the side of the simulation box.

By employing the adjoint method approach instead, we no longer need to check each coordinate to see how the function responds to adding a block. This information is contained in the  $\delta\Theta$ , an array of values corresponding to each coordinate in the domain. By picking the highest value of the array, i.e. placing the dielectric at the coordinate with the greatest number, we are guaranteed to produce the highest change in the function  $\Theta$ . This saves the computational resources and makes certain optimization goals feasible by reducing the simulation time potentially by a factor of  $n^3$ .

## III. PROCEDURE

We want to create a two-dimensional pattern embedded in a three-dimensional region, it is therefore sufficient to generate EM waves that agree with the goal lattice only at the particular plane where the structure resides (say,  $z = 0$ ). Every point in space apart from the region

around the observation slice is thus a potential target for the placement of a dielectric inclusion. Since we want our structure to allow for physical access to the helicity lattice, we leave a margin of  $l$  wavelengths at each side of the  $z = 0$  slice. The simulation space is discretized in the units of wavelength, and any design that we produce can be adapted to an arbitrary length regime as Maxwell's equations are scale invariant. We choose the side length of the inclusion to be the reciprocal of the resolution  $R$ , such that there are  $R$  pixels per wavelength. Upon setting the remaining parameters of our simulation space, we define the normalized (between  $[-1, 1]$ ), analytical expression for the chosen helicity lattice, which we call  $\mathcal{H}_0$ . We define the set  $S$ , containing the minima and maxima of the pattern forming function  $\mathcal{H}_0$ ; in this paper, we chose the control points to be defined as  $\mathbf{r}_p \in \{\mathbf{r}_0, \dots, \mathbf{r}_N\}$  such that  $\mathcal{H}_0(\mathbf{r}_p) > a \cdot \max(\mathcal{H}_0(\mathbf{r}))$  and  $\mathcal{H}_0(\mathbf{r}_p) < a \cdot \min(\mathcal{H}_0(\mathbf{r}))$ , where  $a \in \mathbb{R}_+$ . Naturally, the smaller value chosen for  $a$ , the more points of comparison there will be, and consequently, the resulting field will approximate the goal pattern more closely.

The first step of the optimization process is to run the simulation in the specified region and record the values of the steady-state fields  $\mathbf{E}$  and  $\mathbf{H}$ . We then construct the sources for the adjoint simulation; at each site  $\mathbf{s}_p$ , we place dipoles whose amplitude depends on the steady-state values of the fields and the pattern defined at  $\mathbf{s}_p$ , i.e.  $\mathbf{E}(\mathbf{s}_p), \mathbf{H}(\mathbf{s}_p)$  and  $\mathcal{H}_0(\mathbf{s}_p)$ . At each  $\mathbf{s}_p$ , we position both an electric dipole with the amplitude  $\Delta\mathcal{H}(\mathbf{s}_p)\mathbf{H}^*(\mathbf{s}_p)$ , and a magnetic dipole with the amplitude  $\Delta\mathcal{H}(\mathbf{s}_p)\mathbf{E}^*(\mathbf{s}_p)$ . Running the backward (adjoint) simulation concludes the first step. Upon recording the values of the steady-state fields  $\mathbf{F}$ , we correlate them with the values of  $\mathbf{E}$  as in Eq. (A.10). The result encapsulates the relationship between the placement of a dielectric inclusion and a corresponding change to the merit function  $\Theta$ . In other words, picking a coordinate  $\mathbf{r}_{\max}$  such that  $\text{Re}\{\mathbf{E}(\mathbf{r}_{\max}) \cdot \mathbf{F}(\mathbf{r}_{\max})\}$  is maximum, ensures that placing an inclusion at  $\mathbf{r}_{\max}$  will result in the largest change in  $\Theta$ . We then update the geometry and repeat the previous step until the desired pattern has been achieved.

The procedure involves running two types of simulation (forward and adjoint), and can be summarized in the following way:

1. First stage:
  - (a) Define a 3D simulation space; choose a plane where the 2D helicity pattern is to be created and situate its normalized analytical expression there.
  - (b) In the chosen plane, pick a set  $S$  of critical points  $\mathbf{s}_i$ , where the analytical function is “close” to its absolute maximum values.
  - (c) By running the forward simulation, obtain steady-state values of the fields  $\mathbf{E}$  and  $\mathbf{H}$  at every point in the 3D domain, including the points of interest  $\mathbf{s}_p$ .

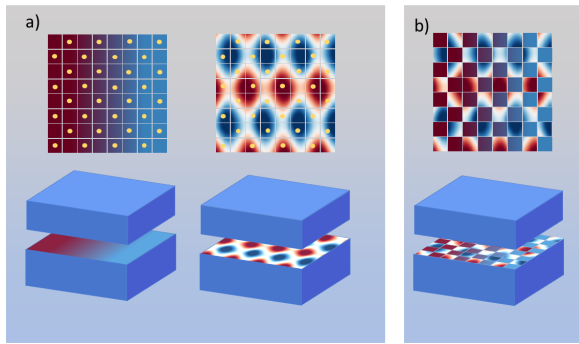


FIG. 3. Simulated field vs the analytical field at a two-dimensional plane embedded in a three-dimensional domain. a) values of the simulated field (left) chosen at control points (yellow) are compared to the analytical values (right) at the same control points. b) successfully optimized simulated field which approximates the values of the analytical field at the control points. This is a simplified visualization where the size of the grid has been exaggerated to present the main idea clearly.

- (d) Place electric and magnetic dipoles at every  $\mathbf{s}_p$  as functions of the  $\mathbf{E}(\mathbf{s}_p)$  and  $\mathbf{H}(\mathbf{s}_p)$  at the first step. Obtain the steady state values of the fields by running the adjoint simulation.
- (e) Correlate the forward and adjoint fields, as in Eq.18. Pick the coordinate where the  $\delta\Theta$  is the highest and place the dielectric inclusion there.

## 2. Second (Iterative) stage:

- (a) Repeat the steps (c)-(e) from the first stage.
- (b) Repeat until the forward field approximates the desired pattern at the chosen plane.

## IV. RESULTS

Using the single beam technique supported by the adjoint method, we have created the patterns approximating the helicity density originally arising as a superposition of three waves in two different configurations. Many other non-interfering superpositions are realizable, and the list of their explicit constituent light sources can be found in [1]. Both lattices were generated using the same parameters of the simulation space and the same number of iterations was run (i.e. resulting structures consist of the same number of blocks). In both cases, we first superposed the collections of plane waves and extracted analytical expressions of the results to form the goal pattern functions. Subsequently, we generated the one-source simulation trying to approximate the analytical results. All simulations were performed using an FDTD library MEEP [29]; the code with detailed documentation can be found in Ref. [30].

### A. Rectangular three wave superposition

The center point of the side of a simulation box is perhaps the most natural choice to place the helicity-generating light source. Since the source plane wave oscillates perpendicular to the lattice's vertical lines of symmetry, the resulting simulation approximates the helicity lattice well (showing clear periodicity by agreeing with the goal pattern at the  $\mathcal{H} = 0$  points) even in lower resolution settings (i.e. less than six pixels per wavelength). The goal structure  $\mathcal{H}_0$ , has the form:

$$\mathcal{H}_0 = \mathcal{N} \cos((2 - \sqrt{2})\pi x) \sin(\sqrt{2}\pi y), \quad (19)$$

where the factor  $\mathcal{N}$  carries the units of  $\varepsilon_0 |E|^2 / 2\omega$ . The analytical solution along with the result of the simulation is shown in Fig. 4. This lattice has two orthogonal lines of symmetry:  $x = n/2(2 - \sqrt{2})$ , and  $y = n/\sqrt{2}$ ,  $n \in \mathbb{N}$ , where  $\mathcal{H}_0$  is zero. The algorithm can thus independently influence the fields along those degrees of freedom more “naturally”, resulting in the outline of the correct structure emerging at an earlier point of the simulation ( $< 100$  iterations). In short, this pattern is well suited to testing the algorithm as it quickly reveals the correct form of the structure.

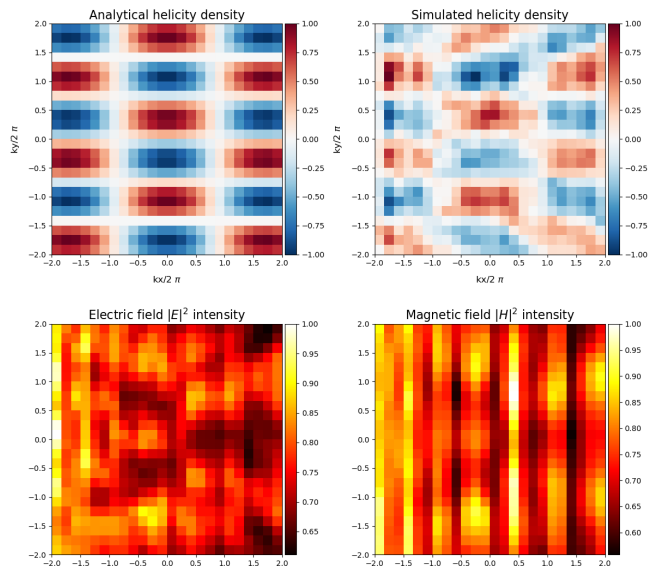


FIG. 4. Comparison between the analytical pattern (upper left panel) and the one-source simulation (upper right panel) for an originally three-wave helicity lattice. The lower panel shows the simulated field's inhomogeneity in the square of the electric (left) and magnetic (right) fields, respectively.

### B. Triangular (diamond) three-wave superposition

The same number of sources as in the previous example, albeit angled differently produces a new lattice. The

analytical expression in this case reads:

$$\mathcal{H}_0 = \mathcal{N} \{-\sin(2\pi x) + \sin(2\pi(x - y)) + \sin(2\pi y)\}, \quad (20)$$

where  $\mathcal{N}$  is the normalization factor keeping the values on the interval  $[-1, 1]$  and carrying the constant  $\varepsilon_0|E|^2/2\omega$ . In contrast to the lattice described by (19), this lattice possesses more than two lines of symmetry. This can be inferred from inspecting the arguments of the sin function in (20); for  $n \in \mathbb{N}$ , lines  $x = n/2, y = n/2$  and  $y = x - n/2$  are the zeroes of  $\mathcal{H}_0$ . As a result, it takes more iterations for the pattern to become apparent as the initial blocks force the simulated lattice to have the zeroes at  $y = x - n/2$ , exploiting the wave nature of the source and modulating the helicity density in the diagonal direction. The other lines of symmetry emerge later as more blocks are added to the structure, approximating the original lattice to a precision controlled by the overall resolution (number of pixels per wavelength). The results of the simulation are plotted in Fig. 5; the geometry of the 3D dielectric crystal is shown in Fig. 7 a).

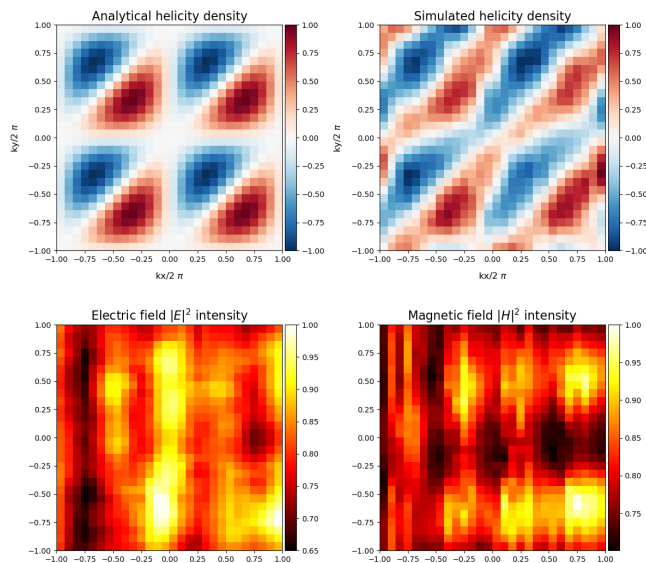


FIG. 5. Comparison between the analytical pattern (upper left panel) and the one-source simulation (upper right panel) for an originally three-wave helicity lattice. The lower panel shows the simulated field’s inhomogeneity in the square of the electric (left) and magnetic (right) fields, respectively

### C. Arbitrary helicity pattern

A helicity density pattern does not have to arise only from superposing light beams with different directions and polarizations. Although an analytical expression in such cases may not exist, the advantage of numerical simulations becomes apparent as any optical pattern is understood by the algorithm as a series of pixels, which

can be applied arbitrarily. The results of the arbitrary helicity density pattern are shown in Fig. 6. Here we simulated the shape of the letter “G”; a grayscale image was normalized between  $[-1, 1]$  to mimic a helicity density. The algorithm was tasked with reproducing this image by simulating the real fields; we note that it correctly distributes the regions of positive and negative helicity density (the inside of the letter “G” is positive), whereas the outline of the letter is close to zero. The shape itself is recognizable, however, some distortion occurs and artifacts are present. The process constructs the base and the top of the “G” first; the “ripples” of positive helicity spread to the bounds of the shape and further details are added successively later. The quality of the resulting lattice is constrained by the size of the simulation volume; such images without periodicity and increased level of detail require a large computational volume. We predict that a complex detailed image (e.g. a portrait) would require the size of the simulation plane to be at least  $200 \times 200$  pixels. Additionally, if one was mostly concerned with the fidelity of the reproduced image, another input beam can be incorporated into the process to improve the quality and speed up the process.

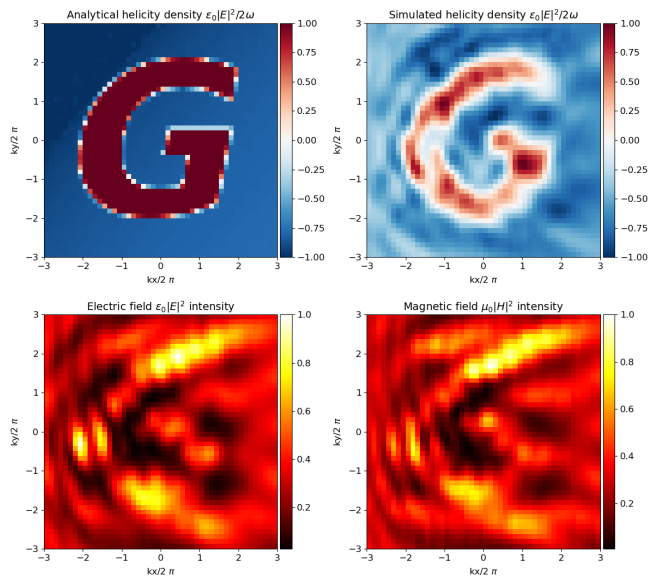


FIG. 6. Comparison between an arbitrary user-defined image (upper left panel) and the one-source simulation (upper right panel) producing a helicity density pattern in the shape of a letter “G”. The lower panel shows the simulated field’s inhomogeneity in the square of the electric (left) and magnetic (right) fields, respectively

## V. ANALYSIS

In the case of analytical solutions for helicity lattices (four sources or fewer),  $\mathbf{E} \cdot \mathbf{E}^*$  can always be made homogeneous [1]. This is not always the case for simu-

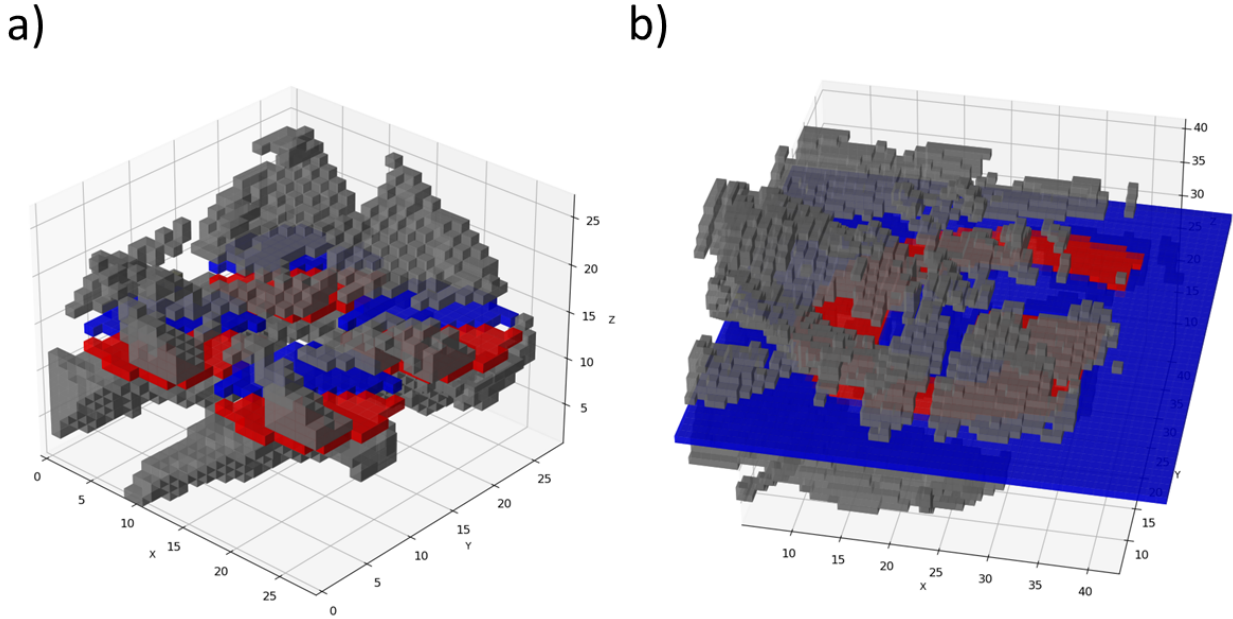


FIG. 7. The three-dimensional models of the crystal-like structure. In a), the arrangement that produces the three-wave triangular (diamond) lattice. In b), the structure that produces an arbitrary pattern (letter “G”). In both cases the gap at the level  $z = 0$  is three wavelengths high.

lated structures and this important detail influences their potential experimental use. As it is widely known, the movement of atoms and molecules in trapping potentials is constrained by optical forces mediated by changes in the electric field. Thus, to create an efficient lattice, one would require the absence of intensity gradients in the region spanned by the structure to allow for interrupted chiral interactions between the enantiomers and the lattice. The fields generated by our simulation possess inhomogeneities due to the finite width of the plane waves generating the helicity. The inhomogeneity is however dependent on the size of a computational vs observational region; the larger the gap between the boundaries of a computational volume and an observation box, the closer the source resembles a plane wave. This, in turn, produces an  $\mathbf{E} \cdot \mathbf{E}^*$  with smaller variations; an infinitely sized computational box would allow one to obtain a perfectly homogenous intensity. Consequently, a trade-off exists between a reasonable computational time and fidelity of the lattice compared to the goal structure. The solution to inhomogeneity in intensity exhibited by arbitrary patterns is unknown. Since they are artificially introduced to be a result of interacting fields, the relationship between their shapes and the resulting intensity gradients is unclear. Future work will address this issue; it will focus on developing more sophisticated methods for producing an arbitrary pattern. An additional merit

function could be defined, specifically controlling the intensity gradients, additionally a weight function between the two merit functions would be introduced. Potentially, a link can be established between certain shapes and the homogeneity of the intensity; this could be revealed by a machine-learning algorithm.

As can be seen in Fig. 7 and discussed in detail in [31], some of the elements of the crystal are “floating”; this can be rectified by running a longer simulation, effectively allowing the algorithm to fill the larger gaps by chance, and then manually removing any “islands” of the dielectric material. Alternatively, a weight function can be implemented so the algorithm is penalized for placing isolated inclusions. A similar issue occurs as the structure is comprised of two halves, allowing for access to the lattice; the crystal can be grown within the bounds of an existing structure providing support, or additional dielectric elements can be incorporated to join the two halves near the edges. As Maxwell’s equations are scale-invariant, so are the helicity lattices. Thus the choice of the size regime dictates the difficulty of potential manufacturing challenges. In our case, we have adopted the nano-scale approach, as it allows us to treat the light sources as plane waves. To pursue the experimental realization, a compromise needs to be found between the computational volume and the order of the wavelength used.

version of the code and Owen Miller for enlightening correspondence.

## VI. CONCLUSIONS/SUMMARY

A gradient-based formalism was used to develop a proof-of-principle scheme capable of reproducing a helicity lattice pattern, only with a reduced number of input sources. The problem was cast as a minimum-seeking algorithm, iteratively growing a crystal-like structure. This object would refract a single beam in such a way as to reproduce the effect of superposing multiple beams, a formation of helicity lattice. We have presented the results of reproducing two, originally three-wave helicity lattices using a single source input. Additionally, we introduced a modified scheme where the pattern to be reproduced was not a result of superposing light sources, but rather an arbitrary image provided by the user. This approach opens up a possibility for designing bespoke helicity patterns suited to the needs of a particular experiment; it is worth mentioning that using the same principles, a different merit function ( $f[\mathbf{E}, \mathbf{H}]$ ) can be provided, thus any desired arrangement of the electric and magnetic fields (not just a helicity lattice) can be achieved.

The simulations reproducing known helicity patterns serve as proof-of-principle concepts and demonstrate the feasibility of using a single light source and a refracting object to mimic the behaviour of a field composed of multiple sources. We have described how increasing the computational volume approximates the plane wave closer and as a result, produces a homogeneous intensity in the case of known helicity patterns. We outlined possible strategies to resolve the issue of intensity gradients in arbitrary patterns. We briefly discussed potential challenges in experimental realizations, especially the manufacturing of the dielectric structure.

## ACKNOWLEDGMENTS

The authors acknowledge financial support from the UK Research and Innovation Council through a doctoral training programme grant (EP-SRC/DTP 2020/21/EP/T517896/1), New Horizons Grant EP/V048449/1 and New Investigator grant EP/W016486/1. The authors also acknowledge fruitful discussions with Stephen M. Barnett, Jörg B. Götte, Ben W. Butler, Thomas M. Jones and Zhujun Ye. We also want to thank Claire Cisowski for testing the early

## Appendix: Variation in the merit function

The monochromatic helicity density composed of  $N$  plane waves is defined as:

$$\mathcal{H}[\mathbf{E}, \mathbf{H}]_{PW} = -\frac{i}{4c\omega} \sum_{i,j=1}^N (\mathbf{E}_i \cdot \mathbf{H}_j^* - \mathbf{E}_i^* \cdot \mathbf{H}_j) e^{(\mathbf{k}_i - \mathbf{k}_j) \cdot \mathbf{r}}. \quad (\text{A.1})$$

For the purposes of derivation of the variation in helicity density, we can use a simplified version:

$$\mathcal{H}[\mathbf{E}, \mathbf{H}] = -\frac{i}{4c\omega} (\mathbf{E} \cdot \mathbf{H}^* - \mathbf{E}^* \cdot \mathbf{H}). \quad (\text{A.2})$$

Given the merit function  $\Theta[\mathbf{E}, \mathbf{H}]$ , which sums over the  $N$  functions at control points  $\mathbf{s}_k$ :

$$\Theta[\mathbf{E}, \mathbf{H}] = \sum_{k=1, \mathbf{s}_k \in S}^N \{ \mathcal{H}_0(\mathbf{s}_k) - \mathcal{H}[\mathbf{E}, \mathbf{H}](\mathbf{s}_k) \}^2, \quad (\text{A.3})$$

we compute the variation  $\delta\Theta$  as:

$$\delta\Theta[\mathbf{E}, \mathbf{H}] = 2 \sum_{k=1, \mathbf{s}_k \in S}^N \Delta\mathcal{H}(\mathbf{s}_k) \delta\mathcal{H}[\mathbf{E}, \mathbf{H}](\mathbf{s}_k), \quad (\text{A.4})$$

$\Delta\mathcal{H}(\mathbf{s}_k)$  being the scalar difference between the simulated field values and the analytical field,  $\mathcal{H}_0(\mathbf{s}_k) - \mathcal{H}[\mathbf{E}, \mathbf{H}](\mathbf{s}_k)$ . We want to evaluate the  $\delta\mathcal{H}[\mathbf{E}, \mathbf{H}]$  at each site in  $S$ . The variation at a site  $\mathbf{r}_p$  will read:

$$\begin{aligned} \delta\mathcal{H}[\mathbf{E}, \mathbf{H}](\mathbf{r}_p) &= \frac{\partial\mathcal{H}(\mathbf{r}_p)}{\partial\mathbf{E}} \delta\mathbf{E} + \frac{\partial\mathcal{H}(\mathbf{r}_p)}{\partial\mathbf{H}} \delta\mathbf{H} + c.c \\ &= \text{Re} [\mathbf{H}^*(\mathbf{r}_p) \delta\mathbf{E}(\mathbf{r}_p) - \mathbf{E}^*(\mathbf{r}_p) \delta\mathbf{H}(\mathbf{r}_p)] \end{aligned} \quad (\text{A.5})$$

The last line was obtained by plugging in the definition of helicity density from (A.2), ignoring the phase and the constant factor, as they are irrelevant to the relative changes in the functional  $\Theta$ . The variations in the fields  $\mathbf{E}$  and  $\mathbf{H}$  can be naturally understood as a difference between the state of the field before an inclusion disturbed it, and the state after. These are given by a product of a Green's tensor  $\mathcal{G}$  with a polarization density  $\mathbf{P}$  induced by introduction of the dielectric block, as given in (13) and (14). Utilizing the reciprocity relations from (7) and (8), we can write the variation in  $\Theta$  at a point  $\mathbf{r}_p$  as:

$$\begin{aligned}
\delta\Theta[\mathbf{E}, \mathbf{H}](\mathbf{s}_p) &= 2\Delta\mathcal{H}(\mathbf{s}_p) \int_{\phi} d^3\mathbf{r} \sum_{i,j=1}^3 \operatorname{Re} \{ H_i^*(\mathbf{s}_p) \mathcal{G}_{ij}^{EP}(\mathbf{r}, \mathbf{s}_p) P_j(\mathbf{r}) + E_i(\mathbf{s}_p) \mathcal{G}_{ij}^{EM}(\mathbf{r}, \mathbf{s}_p) P_j(\mathbf{r}) \} \\
&= 2 \int_{\phi} d^3\mathbf{r} \sum_{i,j=1}^3 \operatorname{Re} \{ P_j(\mathbf{r}) [H_i^*(\mathbf{s}_p) \mathcal{G}_{ij}^{EP}(\mathbf{r}, \mathbf{s}_p) + E_i(\mathbf{s}_p) \mathcal{G}_{ij}^{EM}(\mathbf{r}, \mathbf{s}_p)] \Delta\mathcal{H}(\mathbf{s}_p) \}
\end{aligned} \tag{A.6}$$

Looking closer at (A.6), we see that it is composed of the induced polarization  $\mathbf{P}(\mathbf{r})$  multiplying what we call the adjoint field  $\mathbf{F}_p(\mathbf{r}, \mathbf{s}_p)$ ,

$$\mathbf{F}_p \equiv [\mathbf{H}^*(\mathbf{s}_p) \mathcal{G}^{EP}(\mathbf{r}, \mathbf{s}_p) + \mathbf{E}^*(\mathbf{s}_p) \mathcal{G}^{EM}(\mathbf{r}, \mathbf{s}_p)] \Delta\mathcal{H}(\mathbf{s}_p). \tag{A.7}$$

The field  $\mathbf{F}_p$  contains an electric dipole with amplitude  $\mathbf{H}^*$  and a magnetic dipole with amplitude  $\mathbf{E}$ , both of which are modulated by the difference between the simulated field and the analytical pattern at the point  $\mathbf{s}_p$ ,  $\Delta\mathcal{H}(\mathbf{s}_p)$ . In short, it is an electric field originating from the fictitious electric and magnetic dipoles. Using the fact that  $\mathbf{E}(\mathbf{r}) \propto \mathbf{P}(\mathbf{r})$ , we write the variation in  $\Theta$  at the point  $p$  as:

$$\delta\Theta[\mathbf{E}, \mathbf{H}](\mathbf{s}_p) \approx \operatorname{Re} \{ \mathbf{E}(\mathbf{r}) \cdot \mathbf{F}_p(\mathbf{r}, \mathbf{s}_p) \}, \tag{A.8}$$

making the total variation:

$$\delta\Theta[\mathbf{E}, \mathbf{H}] \approx \operatorname{Re} \left\{ \mathbf{E}(\mathbf{r}) \cdot \sum_p^n \mathbf{F}_p(\mathbf{r}, \mathbf{s}_p) \right\} \tag{A.9}$$

$$= \operatorname{Re} \{ \mathbf{E}(\mathbf{r}) \cdot \mathbf{F}(\mathbf{r}) \}. \tag{A.10}$$

The change in the merit function  $\Theta$  is given by the real part of the overlap between the real  $\mathbf{E}$ , and the adjoint  $\mathbf{F}$  fields.

- 
- [1] K. Kruining, R. Cameron, and J. Götte, Superpositions of up to six plane waves without electric-field interference, *Optica* **5**, 1091 (2018).
- [2] L. Woltjer, A theorem on force-free magnetic fields, *Proceedings of the National Academy of Sciences* **44**, 489 (1958), <https://www.pnas.org/doi/pdf/10.1073/pnas.44.6.489>.
- [3] R. P. Cameron, S. M. Barnett, and A. M. Yao, Optical helicity, optical spin and related quantities in electromagnetic theory, *New Journal of Physics* **14**, 053050 (2012).
- [4] D. Patterson and M. Schnell, New studies on molecular chirality in the gas phase: enantiomer differentiation and determination of enantiomeric excess, *Phys. Chem. Chem. Phys.* **16**, 11114 (2014).
- [5] Y. Tang and A. E. Cohen, Optical chirality and its interaction with matter, *Phys. Rev. Lett.* **104**, 163901 (2010).
- [6] F. Isaule, R. Bennett, and J. B. Götte, Quantum phases of bosonic chiral molecules in helicity lattices, *Physical Review A* **106**, 10.1103/physreva.106.013321 (2022).
- [7] S. Molesky, Z. Lin, A. Y. Piggott, W. Jin, J. Vucković, and A. W. Rodriguez, Inverse design in nanophotonics, *Nature Photonics* **12**, 659 (2018).
- [8] T. Back, U. Hammel, and H.-P. Schwefel, Evolutionary computation: Comments on the history and current state, *IEEE transactions on Evolutionary Computation* **1**, 3 (1997).
- [9] G. F. W. . A. J. Fu M. C., Simulation optimization: a review, new developments, and applications., in *Proc. Winter Simulation Conferenc*, NordiCHI (IEEE, 2005) pp. 83–95.
- [10] M. M. Spuhler, B. J. Offrein, G.-L. Bona, R. Germann, I. Massarek, and D. Erni, A very short planar silica spot-size converter using a nonperiodic segmented waveguide, *Journal of Lightwave Technology* **16**, 1680 (1998).
- [11] D. C. Dobson and S. J. Cox, Maximizing band gaps in two-dimensional photonic crystals, *SIAM Journal on Applied Mathematics* **59**, 2108 (1999).
- [12] T. Felici and H. W. Engl, On shape optimization of optical waveguides using inverse problem techniques, *Inverse problems* **17**, 1141 (2001).
- [13] S. J. Cox and D. C. Dobson, Band structure optimization of two-dimensional photonic crystals in h-polarization, *Journal of Computational Physics* **158**, 214 (2000).
- [14] M. Gerken and D. A. Miller, Multilayer thin-film structures with high spatial dispersion, *Applied Optics* **42**, 1330 (2003).
- [15] C. Y. Kao, S. Osher, and E. Yablonovitch, Maximizing band gaps in two-dimensional photonic crystals by using level set methods, *Applied Physics B* **81**, 235 (2005).
- [16] G. Volpe and R. E. Melnik, The design of transonic aerofoils by a well-posed inverse method, *International Journal for Numerical Methods in Engineering* **22**, 341 (1986).
- [17] P. I. Borel, A. Harpøth, L. H. Frandsen, M. Kristensen, P. Shi, J. S. Jensen, and O. Sigmund, Topology optimization and fabrication of photonic crystal structures, *Optics express* **12**, 1996 (2004).
- [18] J. S. Jensen and O. Sigmund, Systematic design of photonic crystal structures using topology optimization: Low-loss waveguide bends, *Applied physics letters* **84**, 2022 (2004).
- [19] T. P. Xiao, O. S. Cifci, S. Bhargava, H. Chen, T. Gissibl, W. Zhou, H. Giessen, K. C. Toussaint Jr, E. Yablonovitch, and P. V. Braun, Diffractive spectral-splitting optical element designed by adjoint-based electromagnetic optimization and fabricated by femtosecond 3d direct laser writing, *ACS Photonics* **3**, 886 (2016).

- [20] A. Y. Piggott, J. Lu, K. G. Lagoudakis, J. Petykiewicz, T. M. Babinec, and J. Vučković, Inverse design and demonstration of a compact and broadband on-chip wavelength demultiplexer, *Nature Photonics* **9**, 374 (2015).
- [21] D. C. Dobson and L. B. Simeonova, Optimization of periodic composite structures for sub-wavelength focusing, *Applied Mathematics and Optimization* **60**, 133 (2009).
- [22] W. Jin, R. Messina, and A. W. Rodriguez, Overcoming limits to near-field radiative heat transfer in uniform planar media through multilayer optimization, *Optics Express* **25**, 14746 (2017).
- [23] R. Bennett, Inverse design of environment-induced coherence, *Phys. Rev. A* **103**, 013706 (2021).
- [24] J. Matuszak, S. Y. Buhmann, and R. Bennett, Shape optimizations for body-assisted light-matter interactions, *Phys. Rev. A* **106**, 013515 (2022).
- [25] O. Diekmann, D. Lentrodt, and J. Evers, Inverse design approach to x-ray quantum optics with mössbauer nuclei in thin-film cavities, *Phys. Rev. A* **105**, 013715 (2022).
- [26] M. Costabel and F. L. Louër, Shape derivatives of boundary integral operators in electromagnetic scattering. part ii: Application to scattering by a homogeneous dielectric obstacle, *Integral Equations and Operator Theory* **73**, 17 (2011).
- [27] O. Miller, *Photonic Design: From Fundamental Solar Cell Physics to Computational Inverse Design*, Ph.D. thesis, EECS Department, University of California, Berkeley (2012).
- [28] A. Zhan, R. Gibson, J. Whitehead, E. Smith, J. R. Hendrickson, and A. Majumdar, Controlling three-dimensional optical fields via inverse mie scattering, *Science Advances* **5**, eaax4769 (2019), <https://www.science.org/doi/pdf/10.1126/sciadv.aax4769>.
- [29] A. F. Oskooi, D. Roundy, M. Ibanescu, P. Bermel, J. Joannopoulos, and S. G. Johnson, Meep: A flexible free-software package for electromagnetic simulations by the fdd method, *Computer Physics Communications* **181**, 687 (2010).
- [30] R. Kilianski, Inverse design of arbitrary optical helicity structures, <https://researchdata.gla.ac.uk/1374/> (2022).
- [31] Y. Augenstein and C. Rockstuhl, Inverse design of nanophotonic devices with structural integrity, *ACS Photonics* **7**, 2190 (2020), <https://doi.org/10.1021/acsp Photonics.0c00699>.